Reparameterization Approach to Gradient-Based Inverse Design of Three-Dimensional Nanophotonic Devices

Erez Gershnabel, Mingkun Chen, Chenkai Mao, Evan W. Wang, Philippe Lalanne, and Jonathan A. Fan*

ACCESS | Metrics & More | Article Recommendations | SI Supporting Information

ABSTRACT: We propose a three-dimensional freeform nano-photonic platform in which wavelength-scale domains comprise basic geometric structures with explicitly defined dimensions, positions, orientations, and minimum feature size constraints. Given a desired wavefront shaping objective, these parameters can be collectively optimized using gradient-based shape optimization with full accounting of near-field interactions between structures. We apply our concept to a variety of metagratings supporting high diffraction efficiencies and polarization control, and we experimentally demonstrate a device with a tailored polarization response as a function of wavelength. The combination of device capability, feature size constraints, and ease of manufacturability enabled by our methodology will facilitate the development of robust, high performance, nanophotonic technologies.

KEYWORDS: *metasurface, metagrating, reparameterization, freeform optimization, feature size control, polarization control*
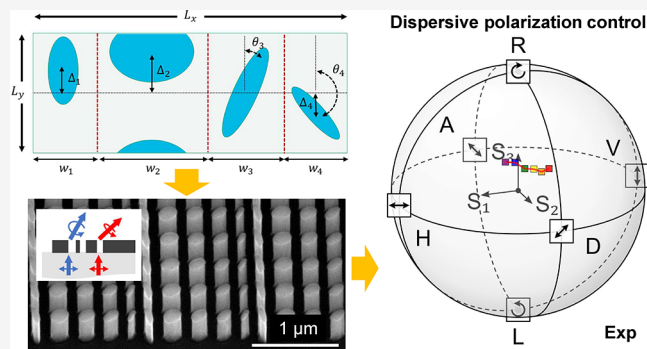
INTRODUCTION

Subwavelength-scale geometric structures that control the shaping, routing, and localization of electromagnetic waves are central to many scientific and technological domains in photonics, including communications,[1,2] detection, imaging, and optical computing.[3] The process of selecting a proper set of structures to achieve a desired optical response remains a challenging and open-ended task because it involves searching through a high-dimensional, nonconvex design space for which brute force searching is intractable. As such, various methods have been developed that balance the complexity of the design procedure with the performance metrics of the final devices.[4,5]

Traditional design methods are based on the utilization of relatively simple geometric layouts, with shapes determined by physical intuition. For metasurfaces, these shapes are based on subwavelength-scale waveguides and resonators that are arranged in a regular lattice to produce a nanoscale phased array. These approaches are widely used because of their interpretable framework and ease of implementation. However, they utilize simplifications, such as the use of basic shapes, a regular lattice, and approximations to near-field interactions between neighboring structures, which can limit device performance. Alternative approaches involve computational methods where the desired optical response is framed as a Figure of Merit (FoM) and maximized using an iterative optimization algorithm.

Such inverse design concepts can enable the design of metasurfaces beyond the capabilities of traditional methods, including devices featuring exceptionally high efficiencies,[6] large numerical apertures,[7] broadband response,[8] and multi-plexed responses[9] as a function of angle and wavelength.

For photonics, the most versatile and computationally efficient inverse design algorithms are based on freeform topology optimization,[10−12] in which every dielectric voxel in the simulation domain is a free parameter that can be modified using the adjoint variables method[13,14] or autodifferentiation.[15,16] The ability for topology optimization to explore exceptionally large design spaces without approximations to Maxwell's equations has led to demonstrations of freeform metagratings,[6,17,18] metalenses,[7,11,12] and on-chip photonic devices[19] with exceptional performance. However, hard minimum feature size tolerances[20−23] and robustness criteria[24−26] can be difficult to incorporate into topology optimized designs, even with heuristic methods that have been developed to address these issues,[27−29,42] and there remain experimental challenges to accurately manufacturing complex freeform shapes. In addition, the operating principles of these devices lack straightforward physical interpretability.
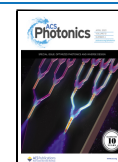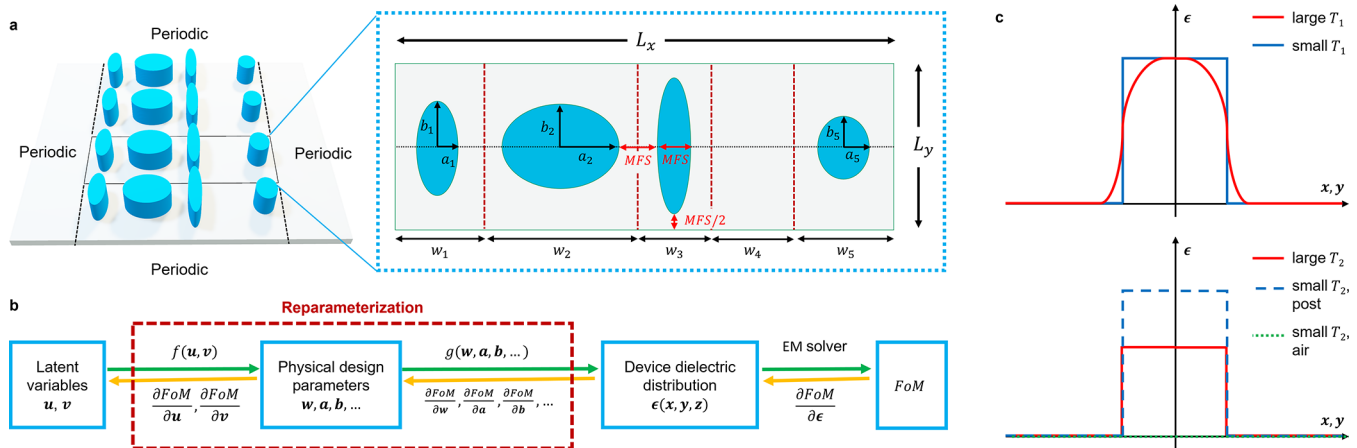
Figure 1. 3D reparameterization concept. (a) Schematic of a freeform metasurface device with periodic boundary conditions and a top view of a single metasurface period featuring nonrotated elliptical metastructures aligned along the x-axis. (b) High level computational graph of the reparameterization procedure and its utilization in gradient-based optimization. (c) Cross sectional plots of dielectric distributions of a metastructure at different values of T_1 and T_2.

Gradient-based design concepts that can produce freeform photonic devices beyond the constraints and simplifications of traditional methods, while also limiting the immense degrees of freedom featured in fully freeform topology optimization, have the potential to combine the best features of traditional and freeform design methods. In this study, we propose an algorithmic design platform in which devices are defined as an ensemble of simple geometric features that are collectively optimized using gradient-based shape optimization. We consider periodic diffractive metasurfaces in this analysis, and the shapes and positions of each feature within the metasurface (Figure 1a) are described in a low dimensional latent space that transform to physical structures, thereby enabling control over the complexity of the design space. As this transformation of latent space device representations to physical devices is fully analytic and differentiable, it can be readily incorporated into a freeform gradient-based device optimization procedure, as illustrated in the computational graph depicted in Figure 1b. These concepts build on prior formalisms recently proposed for the gradient-based optimization of two-dimensional metasurface systems in which the dimensions of subwavelength-scale dielectric ridges were controlled using a reparameterization approach.[30]

Compared to existing photonic device design methods, our concept offers multiple advantages. First, it models the full optimization domain with fullwave physics without approximation, allowing near-field coupling between geometric features to be accounted for and exploited. Second, it allows minimum feature size constraints to be explicitly and robustly defined in the device layout parametrization scheme. Third, the gradient-based design procedure is based on the adjoint variables method, which is computationally efficient and allows the shape of each geometric feature in the domain to be optimized each iteration with only forward and adjoint simulations. Fourth, the specification of basic geometric features help to improve manufacturing accuracy and device robustness beyond the scope of purely freeform devices.

■ 3D REPARAMETERIZATION FORMALISM

Our reparameterization approach considers a device with wavelength-scale domains of lateral dimensions L_x and L_y. Each domain is subdivided into N subcells along the x-axis (Figure 1a), and each subcell comprises an elliptically shaped dielectric feature, which we term a metastructure. This metastructure can take the form of isolated posts, ridges, and air voids within ridges. The feature sizes within and between metastructures are bound by a user-defined minimum feature size, MFS. The subcell widths and the dimensions, positions, and orientations of the metastructures are represented by unconstrained and continuous latent space geometric representations that transform to geometric device parameters using differentiable analytic expressions, discussed below.

The latent variable representation of subcell widths is described by a $1 \times (N-1)$ vector $\mathbf{u}$ that can take values spanning $-\infty$ to ∞. Transforming these latent variables to physical widths w_m, where m is the subcell index, produces a set of cell widths that satisfy the following constraints:

$$\sum_{m=1}^{m=N} w_m = L_x$$
$$w_m \geq w_{\min} \tag{1}$$

$w_{\min}$ is defined as the minimum subcell dimension along the x-axis, where $w_{\min} \geq 2\text{MFS}$. Using a formalism derived in ref 30, the following transformation equations are used:

$$s_i = \text{sigmoid}(u_i) = \frac{e^{u_i}}{e^{u_i}+1}, \quad s_N = 1, \ i = 1, ..., N-1$$

$$t_1 = s_1$$

$$t_i = s_i \sqrt{1 - \sum_{j=1}^{i-1} t_j^2}, \ i = 2, ..., N$$

$$w_m = \frac{t_m}{\sum_{j=1}^{N} t_j}(L - N w_{\min}) + w_{\min}, \quad m = 1, ..., N \tag{2}$$

The latent variable representation of the metastructure features within the unit cells are described by the two-dimensional tensor $\mathbf{v}$. For v_{mn}, m parametrizes the subcell index and n parametrizes particular geometric features. We consider here a simplified reparameterization approach in which the metastructures are dielectric elliptical posts with positions located at the geometric center of the subcells. A formalism that accommodates more geometric degrees of freedom will be

considered later in the study. For the mth subcell, the ellipse axes a_m and b_m are obtained by transforming the latent variables v_{ma} and v_{mb} using the following expressions:

$$a_m = [(w_m/2 - \text{MFS}/2) - \text{MFS}/2]\text{sigmoid}(v_{ma}) + \text{MFS}/2$$
$$b_m = [(L_y/2 - \text{MFS}/2) - \text{MFS}/2]\text{sigmoid}(v_{mb}) + \text{MFS}/2$$
(3)

These transformations ensure that MFS constraints are enforced within the subcell. These axis values are then used to define the continuous dielectric distribution within the mth subcell. For isolated dielectric posts, this expression is

$$\epsilon_m^{\text{post}}(x_m, y_m, a_m, b_m, T_1) = \exp\left(-\left(\frac{x_m^2}{a_m^2} + \frac{y_m^2}{b_m^2}\right)^{1/T_1}\right)$$
$$x \in [-w_m/2, w_m/2], \quad y \in [-L_y/2, L_y/2]$$
(4)

$(x_m, y_m) = (0, 0)$ defines the geometric center of the subcell and the dielectric distribution is normalized such that 1 is the value of the device dielectric material and 0 is air. T_1 is a hyperparameter that enables adiabatic toggling of the dielectric distribution from a grayscale representation (i.e., dielectric values smoothly vary as a function of position) to a binary representation (i.e., the device comprises only the device dielectric material and air), as depicted in Figure 1c.

These dielectric distribution expressions can be modified to capture different topological shapes, which is required for tasks such as topology optimization. For example, the dielectric distribution within a subcell can be toggled between dielectric posts and an air void with the following modification:

$$\epsilon_m^{\text{post/air}} = \text{sigmoid}(v_{mc}/T_2)\epsilon_m^{\text{post}}$$
(5)

v_{mc} is a continuous latent variable representing the topological state of the subcell and T_2 is a hyperparameter. For high T_2 values, the dielectric distribution is grayscale and assumes an intermediate topological state that is a mix of air void and post, and as T_2 decreases, the subcell topology is forced to become either an air void or post (Figure 1c). It is important for these dielectric expressions to be tailored so that local gradients evaluated in the grayscale design space at high T_2 values are helpful in improving the performance of devices represented in the physical discrete design space at small T_2 values. We note that the dielectric distribution describing posts can be readily used to describe other topological layouts. For example, elliptical voids within a dielectric ridge can be described as $\varepsilon_m^{\text{void}} = 1 - \varepsilon_m^{\text{post}}$ and solid ridges $\varepsilon_m^{\text{ridge}}$ are elliptical posts in the limit $b_m \to \infty$. Future work will focus on creating and utilizing handcrafted dielectric expressions that can smoothly toggle between these other metastructure topologies.

We exploit the analytic relationships between the latent and physical space device representations to adapt our reparameterization framework to gradient-based optimization algorithms. To walk through the detailed steps, we will focus here on gradient optimization based on the adjoint variables method, depicted in Figure 1b. The first step is the initialization of the optimization algorithm, in which the latent variables $\boldsymbol{u}$ and $\boldsymbol{v}$ are set to random values between -1 and $+1$. These values are chosen to ensure that the latent variables span a wide physical space upon transformation while also minimizing vanishing gradient issues (i.e., ensuring that changes in latent variables lead to sufficiently appreciable changes in physical parameters).

Iterative gradient-based optimization is then performed. In a given optimization iteration, the latent variables are first transformed to physical parameters, which are used to define $\boldsymbol{\epsilon}$ within the device domain. Gradients to the dielectric distribution g_ϵ, which specify how the dielectric values can be perturbed to improve the FoM, are then evaluated with the adjoint method:[14] a forward and adjoint fullwave simulation of the device is performed to evaluate $\boldsymbol{E}_{\text{fwd}}$ and $\boldsymbol{E}_{\text{adj}}$, respectively, and gradients at each position in the domain are computed. For position $\boldsymbol{r}$, the gradient with respect to dielectric constant is

$$g_\epsilon(\boldsymbol{r}) \equiv \frac{\partial \text{FoM}}{\partial \epsilon(\boldsymbol{r})} \propto \text{real}(\boldsymbol{E}_{\text{fwd}}(\boldsymbol{r}) \cdot \boldsymbol{E}_{\text{adj}}^*(\boldsymbol{r}))$$
(6)

Backpropagation using the chain rule produces FoM gradients with respect to the latent variables (i.e., how the latent variables can be modified in a manner that improves the FoM). As an example, the gradient for v_{ma}, $g_{v_{ma}}$, is computed as

$$g_{v_{ma}} \equiv \frac{\partial \text{FoM}}{\partial v_{ma}} = \frac{\text{FoM}}{\partial \epsilon_m(\boldsymbol{r})} \frac{\partial \epsilon_m(\boldsymbol{r})}{\partial a_m} \frac{\partial a_m}{\partial v_{ma}}$$
(7)

These expressions imply a summation over all positions in subcell m to compute this scalar gradient term. $\frac{\partial \text{FoM}}{\partial \epsilon_m}$ is obtained from the adjoint variables method and $\frac{\partial \epsilon_m}{\partial a_m}$ and $\frac{\partial a_m}{\partial v_{ma}}$ are computed by differentiating the analytic transformation equations. In practice, these gradients are computed using the built-in Pytorch autodifferentiation package.[31] Finally, with gradient terms g_u and g_v, the latent variables are updated. For a local gradient-based optimizer, these updates are performed using algorithms such as vanilla gradient descent or Adam. For global gradient-based optimizers based on the training of a generative network,[42,43] these gradient updates are further backpropagated into the deep network to update its weights.

Toggling T_1 from high to low values over the course of gradient-based optimization can help control how g_ϵ is used to update g_u and g_v.[30] In particular, the $\frac{\partial \epsilon_m}{\partial a_m}$ term in the chain rule functions as a type of spatial filter for gradient information, and T_1 in this expression controls the gradient magnitude and distance from the dielectric boundaries for which g_ϵ contributes to latent variable gradients. High T_1 early in the optimization procedure therefore can promote relatively large changes to the device layout. Later in the optimization, low T_1 enforces a more accurate representation of the binary physical device and limits gradient-based changes to the device layout as small perturbations. Toward the end of optimization binary representation is imposed keeping $T_1 > 0$.

GRADIENT-BASED METAGRATING OPTIMIZATION

To explore the efficacy of our approach in the design of metasurfaces, we initially focus on the freeform optimization of silicon metagratings that selectively diffract normally incident TM-polarized radiation to the +1 order in the xz plane. The devices are on a glass substrate, designed for $\lambda = 850$ nm, and have the following fixed geometric parameters: $d = 430$ nm, $L_x = 1800$ nm, $L_y = 400$ nm, and MFS = 70 nm. To design the devices, 100 adjoint-based local optimizations are performed on random initial grayscale dielectric distributions. Fullwave simulations for these devices and those supporting polarization control in later sections are performed using the rigorous coupled wave analysis solver Reticolo.[32]
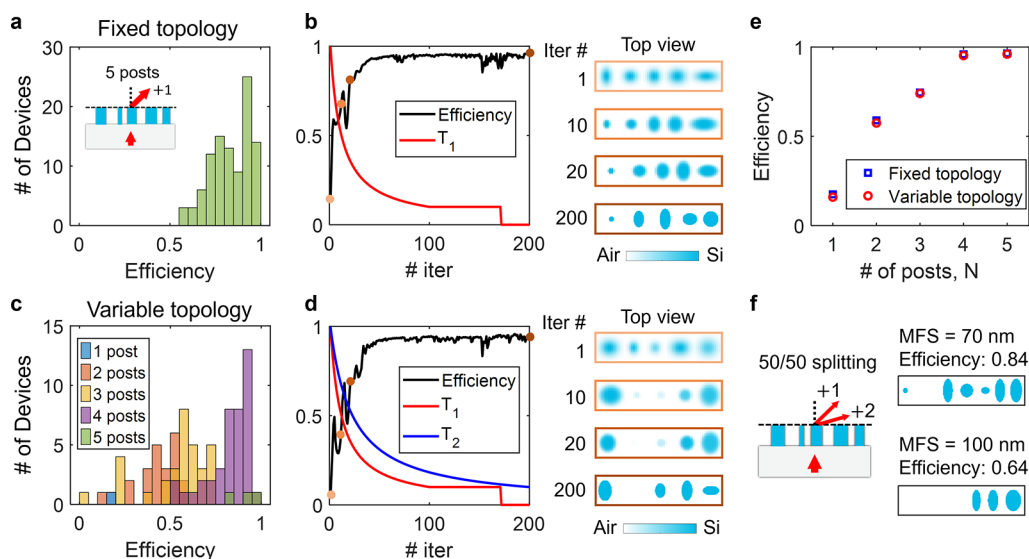
Figure 2. Topology optimization of basic metagrating devices. (a) Histogram of efficiencies of diffractive metagratings obtained by local gradient-based reparameterization optimization. The device topology is fixed to have five dielectric posts. Inset: side view schematic of device function. (b) Optimization trajectory of a representative high performance device from (a). Dielectric distributions at four different points in the design process are also shown. (c) Histogram of efficiencies for diffractive metagratings obtained by local gradient-based reparameterization optimization. The device topology is variable and can possess up to five dielectric posts. (d) Optimization trajectory with variable topology of a representative high performance device. The device is initialized with five grayscale dielectric posts and the final device comprises four silicon posts. (e) Device efficiency versus N for fixed and variable topology-optimized devices. For fixed topology, 100 devices for each N are optimized, and for variable topology, 100 total devices are optimized. The best obtained efficiencies for each design method for each N are shown. (f) Schematic of a multifunctional device that transmits light to the +1 and +2 diffraction orders. Top views and performance metrics of two topology-optimized devices, each with different minimum feature sizes, are shown.
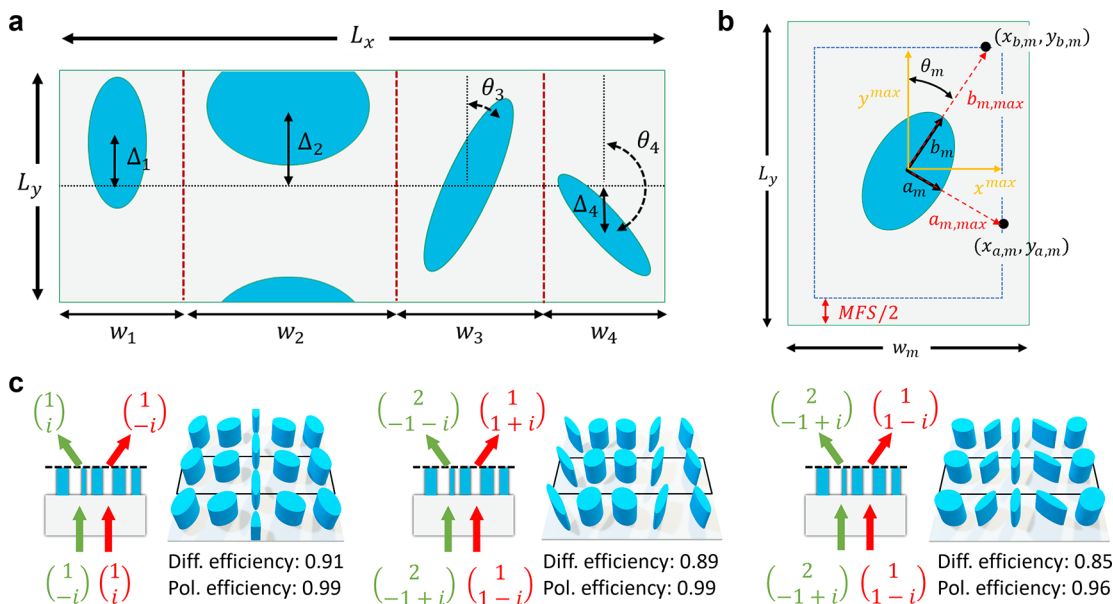

Figure 3. Reparameterization with metastructure symmetry breaking. (a) Single period of a metasurface with elliptical metastructures that can undergo vertical translations and rotations. The metasurface is periodic along the horizontal and vertical axes. (b) Detailed schematic of an individual subcell with geometric parameter labels used in the reparameterization formalism. (c) Device functions, layouts, and theoretical diffraction and polarization efficiency metrics of metasurfaces designed to selectively diffract light to the +1 or −1 order as a function of incident polarization state. The input and output polarization states are written in non-normalized Jones vectors.

We first perform freeform optimization for fixed topology devices comprising five silicon posts. A histogram of the final device efficiencies, shown in Figure 2a, displays a wide distribution of values, indicating that the design landscape is nonconvex and possesses many local optima. The best designed devices have a diffraction efficiency of 96%, which

is near unity and higher than those designed using conventional meta-atom approaches. Diffraction efficiency is defined to be the ratio of radiated power transmitting to the +1 diffraction order to the incident power. An examination of the optimization trajectory of a representative high performance device (Figure 2b) shows that gradient-based calculations

steadily boost device efficiency over the course of optimization, while also evolving the dielectric distribution from grayscale to binary. The final binary device comprises elliptical posts with close spacings, indicating that these devices are accounting for and utilizing near-field coupling between posts to achieve high device performance.

Local freeform optimization of devices with variable topology can also be performed by inclusion of eq 5 in the reparameterization process. A histogram of final device efficiencies sorted by topology (Figure 2c) shows that the optimization algorithm can identify optimal devices with differing numbers of posts. The best devices have either four or five total posts with diffraction efficiencies of 95% and 96%, respectively. The optimization trajectory of a high performing device, displayed in Figure 2d, shows that the initial grayscale dielectric distribution comprising five posts evolves into a binary device with only four posts, with one of the posts shrinking in size and reducing in dielectric contrast over the course of iterative optimization. A comparison of the best devices designed using either fixed or variable topology optimization, as a function of number of posts, is summarized in Figure 2e and indicates that for a given number of posts, each method produces very similar final devices. This indicates that while the design landscapes for fixed and variable topology optimization are different, they support similar local optima and are each suitable for freeform metasurface design.

Our reparameterization platform can readily extend to multiobjective problems. As an example, we consider a metagrating design in which normally incident light is diffracted to the +1 and +2 diffraction orders. Gradient optimization is performed by applying the adjoint variables method to each objective and averaging the computed gradients prior to backpropagation and latent variable updating. Results for the variable topology design of devices with eight subcells, featuring two different minimum feature sizes, are summarized in Figure 2f. For a MFS = 70 nm, the best performing device possesses six dielectric posts and has an average diffraction efficiency of 84%. For a MFS = 100 nm, the best performing device possesses only three dielectric posts and a reduced efficiency of 64%. This model problem indicates the sensitivity of device performance and topology in the presence of hard minimum feature constraints, and it points to the significant benefits afforded by small MFS, which enables engineering of strong near-field coupling between nanostructures.

■ POLARIZATION CONTROL

To further expand the generality our 3D reparameterization scheme, we incorporate two additional mechanisms for metasurface symmetry breaking: metastructure displacements along the y-axis and metastructure angular rotations (Figure 3a). These concepts are essential for enabling new polarization functionality in metasurfaces, which require tailored symmetry breaking to specify the polarization bases of the devices. By combining these added degrees of design freedom with freeform gradient-based optimization, we anticipate our metasurface platform to be capable of matching and extending the functionality of traditional polarization-multiplexed metasurfaces, such as those based on the spin hall effect and geometric phase.

To incorporate y-axis metastructure displacements in each subcell, we introduce the unconstrained latent variable $v_{m\Delta}$ to represent displacement in the mth subcell. This latent representation translates to a physical displacement value, which is bounded by the subcell dimension L_y, with the following expression:

$$\Delta_m = L_y[\text{sigmoid}(v_{m\Delta}) - 1/2] \tag{8}$$

This displacement term is incorporated into eq 4 with the following modification:

$$\epsilon_m^{\text{post}}(x_m, y_m, a_m, b_m, T_1) = \exp\left(-\left(\frac{x_m^2}{a_m^2} + \frac{(y_m - \Delta_m)^2}{b_m^2}\right)^{1/T_1}\right) \tag{9}$$

To account for the angle of rotation of each metastructure, we introduce the latent variable $v_{m\theta}$, which transforms to angular rotations of elliptical features in the mth subcell with the following expression:

$$\theta_m = \text{sigmoid}(v_{m\theta})\pi \tag{10}$$

The maximum angle is bound by π instead of 2π without loss of generality due to the symmetry of the ellipses.

The introduction of metastructure rotations requires a modification to our formalism for MFS incorporation, as these constraints now involve coupled relations involving both a_m and b_m. Our modified subcell with corresponding geometric parameters is shown in Figure 3b for an ellipse centered within the subcell. The MFS constraints produce a usable area delineated by the dashed blue line and are characterized by values $x^{\max}$ and $y^{\max}$: $y^{\max} = \frac{1}{2}(L_y - \text{MFS})$ and $x^{\max} = \frac{1}{2}(w_m - \text{MFS})$. The ellipse axes are a_m and b_m, and the maximum axis lengths, which are extended to and bounded by the dashed blue box, are defined as $a_{m,\max}$ and $b_{m,\max}$, respectively. The spatial position of points defined by $a_{m,\max}$ and $b_{m,\max}$ on the dashed blue box are $(x_{a,m}, y_{a,m})$ and $(x_{b,m}, y_{b,m})$, respectively.

The terms $a_{m,\max}$, $b_{m,\max}$, and their spatial positions are a function of θ_m, $x^{\max}$, and $y^{\max}$ and can be readily defined. We focus on terms pertaining to the positioning of the b_m axis. $x_{b,m}(w_m, \theta_m)$, defined for $x_m \geq 0$ and $0 \leq \theta_m \leq \pi$, can be expressed as

$$x_{b,m}(w_m, \theta_m) = x^{\max}\left[\frac{2}{1 + \exp[y_{b,m}(w_m, \theta_m) - y^{\max}]} - 1\right]$$
$$\times \left[\frac{2}{1 + \exp[-y_{b,m}(w_m, \theta_m) - y^{\max}]} - 1\right] \tag{11}$$

The term $b_{m,\max}$ is a function of b_m, w_m, and θ_m and is defined to be

$$b_{m,\max}(w_m, \theta_m) = \sqrt{x_{b,m}(w_m, \theta_m)^2 + y_{b,m}(w_m, \theta_m)^2} \tag{12}$$

where $y_{b,m}(w_m, \theta_m)$ is defined to be a function of $b_{m,\max}$ and is $y_{b,m}(w_m, \theta_m) = b_{m,\max} \cos(\theta_m)$. Substitution of eq 11 into eq 12 produces a transcendental equation for $b_{m,\max}$, which can be numerically approximated with eq S1 in the Supporting Information. To further ensure the boundaries of the ellipse are within the dashed blue box, we specify $b_{m,\max} \approx \eta f(w_m, \theta_m)$, where η is a hyperparameter <1. Similar steps are used to find $a_{m,\max}$. Finally, these expressions are substituted in a modified eq 3:
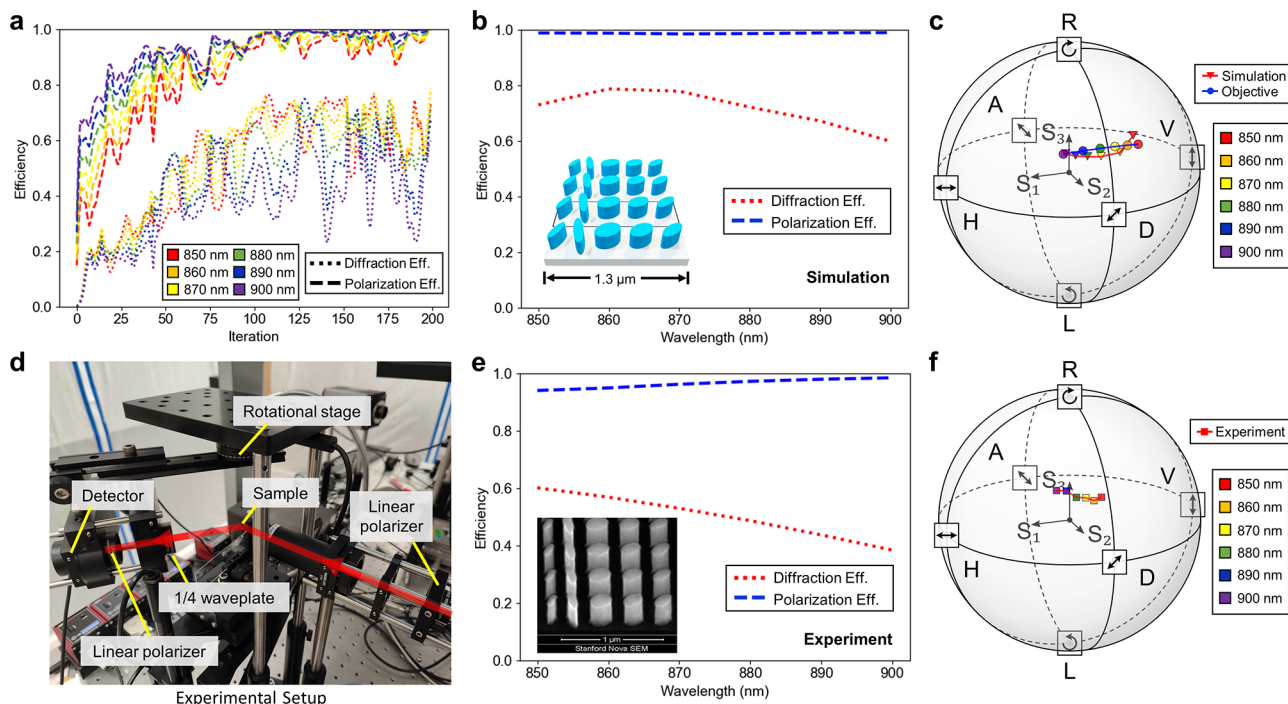
Figure 4. Experimental demonstration of a reparameterized metasurface with polarization functionality. (a) Plot of diffraction and polarization efficiencies as a function of iteration number for a topology-optimized device that diffracts horizontal-polarized incident light to the +1 diffraction order. The target polarizations of the transmitted beam are a function of wavelength and displayed in (c). (b) Plot of theoretical diffraction and polarization efficiencies of the optimized device as a function of wavelength. Inset: device schematic. (c) Target transmitted polarization states and those simulated from the optimized device, as visualized on the Poincare sphere. (d) Experimental setup showing the sample and polarization analyzer. (e) Experimental diffraction and polarization efficiencies as a function of wavelength. Inset: electron microscopy image of the physical device. (f) Experimentally measured polarization states of light transmitted to the +1 order, as visualized on the Poincare sphere.

$$a_m = (a_{m,\max} - \text{MFS}/2)\text{sigmoid}(v_{ma}) + \text{MFS}/2$$

$$b_m = (b_{m,\max} - \text{MFS}/2)\text{sigmoid}(v_{mb}) + \text{MFS}/2 \qquad (13)$$

Importantly, $a_{m,\max}$ and $b_{m,\max}$ are differentiable expressions that are compatible with reparameterized gradient-based device optimization.

To demonstrate the efficacy of this reparameterization approach, we optimize a set of metagratings that can handle arbitrary polarization responses. These devices diffract normally incident light of one polarization state to the +1 order and light of the orthogonal polarization state to the −1 order. The devices can also perform polarization conversion upon transmission. The devices operate at $\lambda = 850$ nm and have geometric parameters matching those discussed in Figure 2, except that $L_x = 1300$ nm. A total of 100 devices are locally optimized with random initialization for each device type, and multiobjective optimization is performed to accommodate the different device functionalities (i.e., diffraction to different orders) for each incident polarization. The performances of these devices are characterized by two terms: diffraction efficiency, which was previously defined, and polarization efficiency, which is defined as $|E_{\text{FoM}}^{\dagger} \cdot E_{\pm 1}|^2$. E_{FoM} and $E_{\pm 1}$ are the normalized Jones vectors of the FoM and physical device, respectively, and $\dagger$ is the conjugate transpose.

Representative metagrating functions, device layouts, and efficiency metrics are summarized in Figure 3c and show that the optimization procedure can produce devices with high diffraction and polarization efficiency. The presented efficiencies are averages of the two different diffraction tasks. Most of the metastructures are aligned along the x-axis due to

symmetry imposed by the normally incident wave, though the device that performs circular polarization conversion incorporates elliptical posts with differing lateral positions. The device on the left diffracts light with a circular polarization basis and is conventionally designed using principles of geometric phase with half waveplate metastructures.[33−37] Our design does not use a geometric phase but nonetheless achieves diffraction and polarization efficiencies similar to those based on a geometric phase. Interestingly, while no explicit symmetry conditions are enforced during the design procedure, the final device converges to one featuring the reflection symmetry. This utilization of reflection symmetry is consistent with the mirror symmetry properties of left- and right-handed circular polarized light and the symmetries built into the desired device function. The two other devices operate with elliptical polarization bases and are conventionally designed by the stitching of asymmetric meta-atoms. Our approach directly produces a wavelength-scale device that accounts for and utilizes near-field coupling between basic symmetry-broken metastructures to achieve high diffraction and polarization efficiencies. As the elliptical polarization bases in these devices do not feature mirror symmetry, these device unit cells do not feature reflection symmetry.

As a final demonstration, we design, fabricate, and characterize a metagrating deflector that supports wavelength-dependent polarization conversion capabilities. Such a device could be used for the polarization shaping of laser pulses, which traditionally utilize bulky setups that involve a series of wavelength-dependent beam splitting, polarization control, and beam combining steps.[38,39] For our demonstration, we consider a metagrating that operates at wavelengths in

the 850 to 900 nm range and that diffracts incident linearly polarized radiation to polarization states specified on the Poincare sphere in Figure 4c. The device comprises five 430 nm-thick polysilicon elliptical posts and has a MFS set to 70 nm. Multiobjective optimization is performed at six discrete wavelengths, uniformly spaced within the 850−900 nm range, to maximize diffraction and polarization efficiency across this entire bandwidth. The optimization trajectories for polarization efficiency as a function of iteration number are shown in Figure 4a and indicate that gradient-based optimization is able to effectively produce a device with near unity polarization efficiency across the full wavelength band. Theoretical diffraction efficiencies of the device are summarized in Figure 4b and display high values.

A comparison of our reparameterized device with fully freeform metagratings indicates that the design space simplifications imposed by our reparameterization method minimally impact device performance. To compare the two design strategies, we perform fully freeform optimization of the metagrating using classical freeform adjoint optimization. The results are summarized in Figure S1 and indicate that the highest performing device from a batch of fully freeform gradient-optimized devices has comparable theoretical diffraction and polarization efficiencies as our reparameterized device. Unlike our device, the high performing freeform device possesses a complex geometric layout that can present experimental fabrication challenges. Furthermore, due to the difficulty of enforcing explicit minimum feature size constraints with this method, the fully freeform device contains a sub-50 nm air gap feature. This side-by-side comparison indicates the potential for reparameterization to dramatically simplify freeform metasurface device layouts without significant reductions in device performance.

Dielectric metagratings are fabricated from a polysilicon film grown on a fused silica substrate. Hydrogen silsesquioxane (HSQ) is used as a hard mask material and is patterned using electron beam lithography, and high aspect ratio silicon pillars are etched using reactive ion etching. The devices are characterized using a supercontinuum laser coupled to a monochromator, and the outputted polarization states are quantified with a polarization analyzer (Figure 4d). An electron microscopy image of a representative device is shown in Figure 4e and shows high aspect ratios elliptical metastructures with straight side walls and shapes consistent with the theoretical design. The experimental polarization efficiencies, summarized in Figure 4e,f, indicate that the experimental device has near unity polarization efficiencies, with positions on the Poincare sphere that nearly match those in Figure 4c. The diffraction efficiencies are not as high as theoretical values, with most efficiency loss due to radiation transmitting through the zeroth order diffraction channel. We hypothesize that the presence of residual HSQ and fabrication imperfections due to local proximity errors and etching inhomogeneity are responsible for this reduced diffraction efficiency.

CONCLUSIONS

In summary, we have demonstrated a three-dimensional reparameterization scheme for metasurfaces that enables the description of freeform wavelength-scale unit cells with hard physical constraints. With this scheme, gradient-based optimization of coupled metastructures can be performed in a straightforward manner, accounting for and utilizing near-field coupling to achieve a desired beam forming task.

Symmetry breaking via metastructure translation and rotation enables polarization control capabilities, which we experimentally demonstrate for a device that converts incident light to different polarization states as a function of wavelength.

Future work will include the extension of reparameterization to differing metasurface topological features and to fully aperiodic unit cells with irregular metastructure placements. Structures with different topologies support complementary wavelength and polarization dispersion properties,[40] and their incorporation into our platform can enable devices with new broadband and multiwavelength capabilities. With aperiodic unit cells, metastructure unit cells can be optimized with tailored scattering profiles[7] and stitched together to produce large area functional devices for high efficiency wavefront engineering and polarization control.

We also anticipate that the specification of metasurface layouts with a reparameterization scheme, which produces a significant dimensionality reduction in the metasurface design space, will also enable other complementary algorithms to more effectively operate. These algorithms include high speed surrogate electromagnetic solvers, such as WaveY-Nets,[41] which can dramatically accelerate the local and global[42−44] gradient-based optimization of metasurface devices. They also include deep networks that can correct for systematic fabrication errors such as proximity error from device patterning and etching. Reduced design spaces particularly benefit deep learning algorithms, where such data regularization can dramatically improve algorithm accuracy and generalizability.

◾ ASSOCIATED CONTENT

Ⓢ Supporting Information

The Supporting Information is available free of charge at https://pubs.acs.org/doi/10.1021/acsphotonics.2c01160.

> Functional approximation for $f(w_m, \theta_m)$; Benchmarking reparameterized freeform devices with fully freeform topology-optimized devices; Figure S1 (PDF)

◾ AUTHOR INFORMATION

Corresponding Author

Jonathan A. Fan − *Department of Electrical Engineering, Stanford University, Stanford, California 94305, United States;* ⓘ orcid.org/0000-0001-9816-9979; Phone: +1(650) 7230278; Email: jonfan@stanford.edu

Authors

Erez Gershnabel − *Department of Electrical Engineering, Stanford University, Stanford, California 94305, United States; Israel Aerospace Industries, Ben Gurion International Airport, Lod 7010000, Israel*

Mingkun Chen − *Department of Electrical Engineering, Stanford University, Stanford, California 94305, United States;* ⓘ orcid.org/0000-0001-9796-0021

Chenkai Mao − *Department of Electrical Engineering, Stanford University, Stanford, California 94305, United States*

Evan W. Wang − *Department of Electrical Engineering, Stanford University, Stanford, California 94305, United States*

Philippe Lalanne − *Laboratoire Photonique, Numérique et Nanosciences, CNRS, Institut d'Optique Graduate School,*

Univ. Bordeaux, F-33400 Talence, France; ● orcid.org/
0000-0003-1979-2290

Complete contact information is available at:
https://pubs.acs.org/10.1021/acsphotonics.2c01160

■ REFERENCES

(1) Thomson, D.; et al. Roadmap on silicon photonics. *J. Opt.* **2016**, *18*, 073003.

(2) Cheng, Q.; Bahadori, M.; Glick, M.; Rumley, S.; Bergman, K. Recent advances in optical technologies for data centers: a review. *Optica* **2018**, *5*, 1354−1370.

(3) O'Brien, J. L.; Furusawa, A.; Vuckovic, J. Photonic quantum technologies. *Nat. Photonics* **2009**, *3*, 687−695.

(4) Kim, W. J.; O'Brien, J. D. Optimization of a two-dimensional photonic-crystal waveguide branch by simulated annealing and the finite-element method. *J. Opt. Soc. Am. B* **2004**, *21*, 289−295.

(5) Shi, Y.; Li, W.; Raman, A.; Fan, S. Optimization of multilayer optical films with a memetic algorithm and mixed integer programming. *ACS Photonics* **2018**, *5*, 684−691.

(6) Sell, D.; Yang, J.; Doshay, S.; Yang, R.; Fan, J. A. Large-angle, multifunctional metagratings based on freeform multimode geometries. *Nano Lett.* **2017**, *17*, 3752−3757.

(7) Phan, T.; Sell, D.; Wang, E. W.; Doshay, S.; Edee, K.; Yang, J.; Fan, J. A. High-efficiency, large-area, topology-optimized metasurfaces. *Light: Science & Applications* **2019**, *8*, 48.

(8) Wang, E. W.; Phan, T.; Yu, S.; Dhuey, S.; Fan, J. A. Dynamic circular birefringence response with fractured geometric phase metasurface systems. *Proc. Natl. Acad. Sci. U. S. A.* **2022**, *119*, No. e2122085119.

(9) Sell, D.; Yang, J.; Doshay, S.; Fan, J. Periodic Dielectric Metasurfaces with High-Efficiency, Multiwavelength Functionalities. *Advanced Optical Materials* **2017**, *5*, 1700645.

(10) Lalau-Keraly, C. M.; Bhargava, S.; Miller, O. D.; Yablonovitch, E. Adjoint shape optimization applied to electromagnetic design. *Opt. Express* **2013**, *21*, 21693−21701.

(11) Bayati, E.; Pestourie, R.; Colburn, S.; Lin, Z.; Johnson, S. G.; Majumdar, A. Inverse designed metalenses with extended depth of focus. *ACS Photonics* **2020**, *7*, 873−878.

(12) Chung, H.; Miller, O. D. High-NA achromatic metalenses by inverse design. *Opt. Express* **2020**, *28*, 6945−6965.

(13) Fan, J. A. Freeform metasurface design based on topology optimization. *MRS Bull.* **2020**, *45*, 196−201.

(14) Hughes, T. W.; Minkov, M.; Williamson, I. A.; Fan, S. Adjoint method and inverse design for nonlinear nanophotonic devices. *ACS Photonics* **2018**, *5*, 4781−4787.

(15) Minkov, M.; Williamson, I. A.; Andreani, L. C.; Gerace, D.; Lou, B.; Song, A. Y.; Hughes, T. W.; Fan, S. Inverse design of photonic crystals through automatic differentiation. *ACS Photonics* **2020**, *7*, 1729−1741.

(16) Hughes, T. W.; Williamson, I. A.; Minkov, M.; Fan, S. Forward-Mode differentiation of Maxwell's equations. *ACS Photonics* **2019**, *6*, 3010−3016.

(17) Sell, D.; Yang, J.; Wang, E.; Phan, T.; Doshay, S.; Fan, J. Ultra-High-Efficiency Anomalous Refraction with Dielectric Metasurfaces. *ACS Photonics* **2018**, *5*, 2402−2407.

(18) Yang, J.; Sell, D.; Fan, J. Freeform metagratings based on complex light scattering dynamics for extreme, high efficiency beam steering. *Annalen der Physik* **2018**, *530*, 1700302.

(19) Molesky, S.; Lin, Z.; Piggott, A. Y.; Jin, W.; Vucković, J.; Rodriguez, A. W. Inverse design in nanophotonics. *Nat. Photonics* **2018**, *12*, 659−670.

(20) Yablonovitch, E.; Vrijen, R. B. Optical projection lithography at half the Rayleigh resolution limit by two-photon exposure. *Nonlinear Optics '98. Materials, Fundamentals and Applications Topical Meeting*; Univ. of California, LA, 1998; pp 126−128.

(21) Joy, D. C. The spatial resolution limit of electron lithography. *Microelectron. Eng.* **1983**, *1*, 103−119.

(22) Wu, B.; Kumar, A.; Pamarthy, S. High aspect ratio silicon etch: A review. *J. Appl. Phys.* **2010**, *108*, 051101.

(23) Marty, F.; Rousseau, L.; Saadany, B.; Mercier, B.; Français, O.; Mita, Y.; Bourouina, T. Advanced etching of silicon based on deep reactive ion etching for silicon high aspect ratio microstructures and three-dimensional micro-and nanostructures. *Microelectron. J.* **2005**, *36*, 673−677.

(24) Wang, E. W.; Sell, D.; Phan, T.; Fan, J. A. Robust design of topology-optimized metasurfaces. *Opt. Mater. Express* **2019**, *9*, 469−482.

(25) Wang, F.; Jensen, J. S.; Sigmund, O. Robust topology optimization of photonic crystal waveguides with tailored dispersion properties. *J. Opt. Soc. Am. B* **2011**, *28*, 387−397.

(26) Schevenels, M.; Lazarov, B. S.; Sigmund, O. Robust topology optimization accounting for spatially varying manufacturing errors. *Computer Methods in Applied Mechanics and Engineering* **2011**, *200*, 3613−3627.

(27) Frei, W.; Tortorelli, D. A.; Johnson, H. T. Geometry projection method for optimizing photonic nanostructures. *Opt. Lett.* **2007**, *32*, 77−79.

(28) Khoram, E.; Qian, X.; Yuan, M.; Yu, Z. Controlling the minimal feature sizes in adjoint optimization of nanophotonic devices using bspline surfaces. *Opt. Express* **2020**, *28*, 7060−7069.

(29) Vercruysse, D.; Sapra, N. V.; Su, L.; Trivedi, R.; Vučković, J. Analytical level set fabrication constraints for inverse design. *Sci. Rep.* **2019**, *9*, 1−7.

(30) Chen, M.; Jiang, J.; Fan, J. A. Design space reparameterization enforces hard geometric constraints in inverse-designed nanophotonic devices. *ACS Photonics* **2020**, *7*, 3141−3151.

(31) Paszke, A.; Gross, S.; Massa, F.; Lerer, A.; Bradbury, J.; Chanan, G.; Killeen, T.; Lin, Z.; Gimelshein, N.; Antiga, L. Pytorch: An imperative style, high-performance deep learning library. *Advances in Neural Information Processing Systems* **2019**, 8026−8037.

(32) Hugonin, J. P.; Lalanne, P. *Reticolo software for grating analysis*; Institut d'Optique: Orsay, France, 2005.

(33) Pancharatnam, S. Generalized theory of interference and its applications. *Proc. Indian Acad. Sci. A* **1956**, *44*, 247−262.

(34) Berry, M. Quantal phase factors accompanying adiabatic changes. *Proc. R. Soc. A* **1984**, *392*, 45−57.

(35) Balthasar Mueller, J. P.; Rubin, N. A.; Devlin, R. C.; Groever, B.; Capasso, F. Metasurface polarization optics: independent phase control of arbitrary orthogonal states of polarization. *Phys. Rev. Lett.* **2017**, *118*, 113901.

(36) Rubin, N. A.; Shi, Z.; Capasso, F. Polarization in diffractive optics and metasurfaces. *Adv. Opt. Photonics* **2021**, *13*, 836−970.

(37) Cohen, E.; Larocque, H.; Bouchard, F.; Nejadsattari, F.; Gefen, Y.; Karimi, E. Geometric phase from Aharonov−Bohm to Pancharatnam−Berry and beyond. *Nat. Rev. Phys.* **2019**, *1*, 437−449.

(38) Divitt, S.; Zhu, W.; Zhang, C.; Lezec, H. J.; Agrawal, A. Ultrafast optical pulse shaping using dielectric metasurfaces. *Science* **2019**, *364*, 890−894.

(39) Misawa, K. Applications of polarization-shaped femtosecond laser pulses. *Adv. Phys.: X.* **2016**, *1*, 544−569.

(40) Shrestha, S.; Overvig, A.; Lu, M.; Stein, A.; Yu, N. Broadband achromatic dielectric metalenses. *Light Sci. Appl.* **2018**, *7*, 85.

(41) Chen, M.; Lupoiu, R.; Mao, C.; Huang, D. H.; Jiang, J.; Lalanne, P.; Fan, J. A. High speed simulation and freeform optimization of nanophotonic devices with physics-augmented deep learning. *ACS Photonics* **2022**, *9*, 3110−3123.

(42) Jiang, J.; Fan, J. A. Simulator-based training of generative neural networks for the inverse design of metasurfaces. *Nanophotonics* **2019**, *9*, 1059−1069.

(43) Jiang, J.; Fan, J. A. Global optimization of dielectric metasurfaces using a physics-driven neural network. *Nano Lett.* **2019**, *19*, 5366−5372.

(44) Chen, M.; Jiang, J.; Fan, J. A. Algorithm-driven paradigms for freeform optical engineering. *ACS Photonics* **2022**, *9*, 2860−2871.